



A 4 × 4 cm² Nanoengineered Solid Oxide Electrolysis Cell for Efficient and Durable Hydrogen Production

Tong, Xiaofeng; Ovtar, Simona; Brodersen, Karen; Hendriksen, Peter Vang; Chen, Ming

Published in:
A C S Applied Materials and Interfaces

Link to article, DOI:
[10.1021/acsami.9b07749](https://doi.org/10.1021/acsami.9b07749)

Publication date:
2019

Document Version
Peer reviewed version

[Link back to DTU Orbit](#)

Citation (APA):
Tong, X., Ovtar, S., Brodersen, K., Hendriksen, P. V., & Chen, M. (2019). A 4 × 4 cm² Nanoengineered Solid Oxide Electrolysis Cell for Efficient and Durable Hydrogen Production. *A C S Applied Materials and Interfaces*, 11(29), 25996-26004. <https://doi.org/10.1021/acsami.9b07749>

General rights

Copyright and moral rights for the publications made accessible in the public portal are retained by the authors and/or other copyright owners and it is a condition of accessing publications that users recognise and abide by the legal requirements associated with these rights.

- Users may download and print one copy of any publication from the public portal for the purpose of private study or research.
- You may not further distribute the material or use it for any profit-making activity or commercial gain
- You may freely distribute the URL identifying the publication in the public portal

If you believe that this document breaches copyright please contact us providing details, and we will remove access to the work immediately and investigate your claim.

A 4×4 cm² Nano-Engineered Solid Oxide Electrolysis Cell for Efficient and Durable Hydrogen Production

*Xiaofeng Tong, Simona Ovtar, Karen Brodersen, Peter Vang Hendriksen, Ming Chen**

Department of Energy Conversion and Storage, Technical University of Denmark,
Frederiksborgvej 399, Roskilde, DK-4000, Denmark

ABSTRACT: Despite various advantages of high-temperature solid oxide electrolysis cells (SOECs) over their low-temperature competitors, the insufficient long-term durability has prevented the commercialization of SOECs. Here, we address this challenge by employing two nano-engineered electrodes. The O₂-electrode consists of a La_{0.6}Sr_{0.4}CoO_{3- δ} (LSC) and Gd,Pr-co-doped CeO₂ (CGPO) nanocomposite coating deposited on a Gd-doped CeO₂ (CGO) scaffold, and the H₂-electrode comprises a Ni/yttria stabilized zirconia (YSZ) electrode modified with a nano-granular CGO coating. The resulting cell with an active area of 4×4 cm² exhibits a current density exceeding 1.2 A cm⁻² at 1.3 V and 750 °C for steam electrolysis, while also offering excellent long-term durability at 1 A cm⁻² with a high steam-to-hydrogen conversion of ~56%. We further unravel the degradation mechanism of the most commonly used Ni/YSZ electrode at these conditions and describe the mitigation of the discussed mechanism on our nano-engineered

electrode. Our findings demonstrate the potential of designing robust SOECs by nano-engineering electrodes through infiltration, and have significant implications for the practical integration of SOEC technology in the future sustainable energy system.

KEYWORDS: solid oxide electrolysis cell, hydrogen, infiltration, durability, hydrogen evolution reaction, oxygen evolution reaction

Introduction

Electrochemical water splitting using surplus electricity from renewable sources (the so-called “power-to-gas” (P2G) technology) has the potential to address energy storage challenge and to offer a green solution for hydrogen (H_2) production.¹ While the low-temperature (typically 50–100 °C) alkaline electrolysis cells (AECs) and polymer electrolyte membrane electrolysis cells (PEMECs) are already commercially available, reversing the operation of high-temperature (typically 650–950 °C) solid oxide fuel cells (SOFCs) as solid oxide electrolysis cells (SOECs, Figure 1) has received increasing attention in recent years due to their unique advantages. Unlike low-temperature cells, high-temperature SOEC operation enables high efficiency at high production rate. Current densities exceeding 1 A cm^{-2} are regularly reported at close to 100% efficiency (at a thermal-neutral voltage of 1.29 V).^{2–5} Besides, high operating temperature avoids using noble metal based catalysts (as for PEMECs) and enables utilizing a variety of waste heat sources.

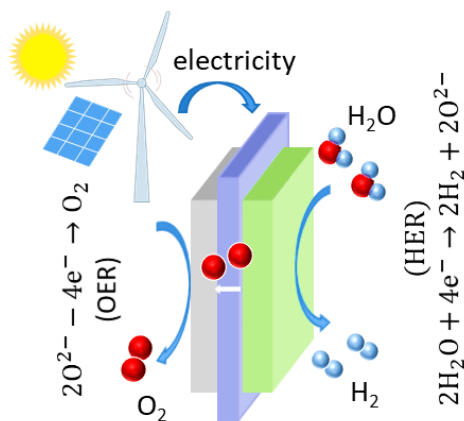


Figure 1. Schematic of water splitting using SOECs. When renewable electricity is applied, water/steam is split, releasing H_2 at the H_2 -electrode (hydrogen evolution reaction, HER). The

oxygen ion is driven across the electrolyte, releasing O₂ at the O₂-electrode (oxygen evolution reaction, OER).

Despite these advantages, the insufficient long-term durability has prevented the commercialization of SOECs. Conventional SOECs consists of a thin yttria-stabilized zirconia (YSZ) electrolyte, a strontium-doped lanthanum manganite (LSM)/YSZ composite O₂-electrode and a Ni/YSZ H₂-electrode. The reported durability on such SOECs has been disappointing, particularly when operated at above 0.5 A cm⁻². For example, Graves et al.⁶ reported a degradation rate of 0.952 V kh⁻¹ for a 420 h testing period at 1 A cm⁻² (the cell voltage increased from 1.33 V to 1.73 V, corresponding to an efficiency decrease from 96% to 75%). Even at 0.7 A cm⁻², Hartvigsen et al.⁷ reported an increase in the cell resistance from 0.50 to 0.62 Ω cm² for 300 h operation, corresponding to a cell voltage increase of approximately 0.28 V kh⁻¹. In most studies, a key degradation mechanism has been reported as microstructural damage near the LSM/YSZ electrode – YSZ electrolyte interface.^{6,8-15} Graves et al.⁶ found that this microstructural damage can be eliminated by using a reversible cycle with periods of 1 h in electrolysis mode and 5 h in fuel-cell mode, but such a cycle does not fit the flexibility requirement for practical applications. Benefiting from the development in SOFCs, mixed ionic-electronic conducting (MIEC) oxides have emerged as alternative O₂-electrode materials in SOECs, and infiltration (also known as impregnation) has been used as a route to prepare such MIEC type O₂-electrodes (Table S1).¹⁶⁻¹⁸ Nevertheless, most studies on infiltrated cells focused on mainly improving initial performance and were carried out at button cell level with an active area less than 2 cm², only few concentrated on issues related to durability and scale-up.

More importantly, the Ni/YSZ H₂-electrodes, which display excellent activity for the HER, have also been reported to show severe microstructural degradations at high current densities, likely associated with Ni coarsening and migration and even the reduction of YSZ leading to formation of ZrO₂ nano-particles on the Ni surface.¹⁹⁻²⁸ Though alternative perovskite oxides have been explored as H₂-electrodes, the activity for the HER and performance of these oxides have not reached the levels observed for that of the Ni/YSZ electrodes (Table S2). Our recent work has demonstrated mitigation of the Ni migration in Ni/YSZ electrode by microstructure optimization, reducing degradation rate from ~ 0.250 V kh⁻¹ to ~ 0.060 V kh⁻¹ when operating at 1 A cm⁻² and 800 °C.²³ More recently, we have found that surface modification by coating nano-sized electrocatalysts as another effective way for durability enhancement, reducing degradation rate from 0.699 V kh⁻¹ to 0.114 V kh⁻¹ at 1.25 A cm⁻² and 800 °C.²⁹ However, further improvement in durability is required.

In this work, we report on a cell architecture demonstrated at 4×4 cm² level (active area) with two nano-engineered electrodes, prepared via conventional techniques of ceramic processing and infiltration. The O₂-electrode consists of a La_{0.6}Sr_{0.4}CoO_{3-δ} (LSC) and Gd,Pr-codoped CeO₂ (CGPO) nanocomposite coating deposited on a Gd-doped CeO₂ (CGO) scaffold (herefrom referred to as LSC-CGPO-CGO). LSC was selected as the catalyst for OER due to its excellent mixed ionic and electronic conductivity and fast oxygen exchange kinetics.³⁰ The H₂-electrode comprises a Ni/YSZ electrode surface modified with a nanogranular CGO coating (herefrom referred to as CGO-Ni/YSZ). This is motivated by the more active oxygen exchange kinetics and redox capacity of CeO₂ and its derivatives (including CGO) in comparison to YSZ.³¹⁻³³ The cell exhibits a current density exceeding 1.2 A cm⁻² at 1.3 V and 750 °C for steam electrolysis, while also offering excellent long-term durability at 1 A cm⁻² with a steam-to-hydrogen conversion of $\sim 56\%$.

Results and discussion

Full cell design. First, H₂-electrode-supported cells with a configuration NiO/YSZ support | NiO/YSZ H₂-electrode | YSZ electrolyte | CGO barrier | porous CGO layer, were fabricated by laminating and co-firing tape-casted green sheets at 1315 °C. The original size of the cells after sintering was 12×12 cm². From this smaller pieces (5.3×5.3 cm²) for testing were cut by laser cutting (Figure 2a). Figure 2b shows typical cross-sectional scanning electron microscope (SEM) image of these cells. Note that the NiO/YSZ side of the cells has been reduced to Ni/YSZ prior to the imaging.

On the basis of these cells, one cell with two nano-engineered electrodes (named as Cell A, Figure S1) was prepared by infiltrating LSC-CGPO nanocomposites into the CGO scaffold and infiltrating CGO into the pre-reduced Ni/YSZ (further details about infiltration is available in the supporting information). Figure 2d,f shows that the LSC-CGPO covered the internal surfaces of the CGO scaffold well and also seems well interconnected. Figures 2e,g illustrate the microstructure of the Ni/YSZ prior to and after coating with CGO. The CGO nanoparticles were well deposited on the surface of both Ni and YSZ, and in great concentration at the three-phase boundaries (TPBs) where Ni, YSZ, and gas are in contact. This was further evidenced by the corresponding energy-dispersive X-ray spectroscopy (EDX) where strongest Ce signals are found at Ni/YSZ/pore lines (Figure S2). These TPBs are the key interfaces that largely govern the performance of Ni/YSZ H₂-electrode and are also where the degradation phenomena are primarily observed. For comparison, one cell with the same LSC-CGO-CGO O₂-electrode but without CGO infiltration on Ni/YSZ (named as Cell B) was also prepared.

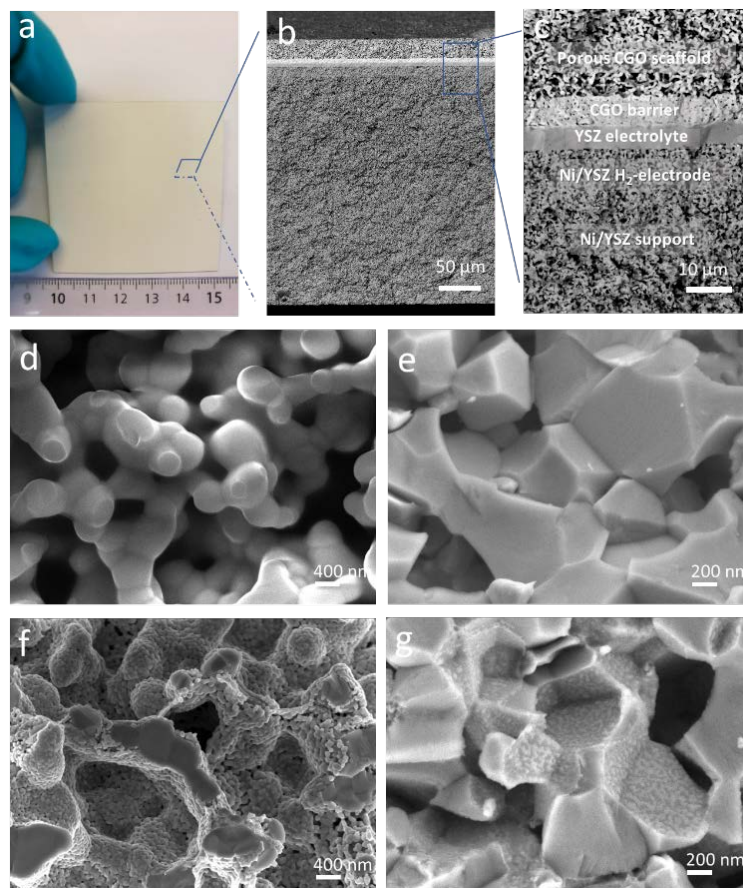


Figure 2. (a) A photo and (b,c) SEM images of the H₂-electrode-supported cells. Cross-sectional SEM images of (d) porous CGO scaffold, (e) Ni/YSZ H₂-electrode, (f) CGO scaffold deposited with LSC and CGPO nanocomposite (LSC-CGPO-CGO O₂-electrode) and (g) Ni/YSZ H₂-electrode after CGO infiltration (CGO-Ni/YSZ H₂-electrode).

Performance evaluation. The prepared cells were tested using in-house built testing rigs. The active area of the cells was 4×4 cm². The edges were used for sealing (experimental details on the testing are provided in the supporting information). Figure 3a shows the current-voltage (*I*-*V*) curves of the electrolysis cells measured at 800–700 °C with 50%H₂O-50%H₂ fed to the H₂-electrode and dry air to the O₂-electrode. The open-circuit voltages (OCVs) of the cells are all

within 10 mV off the calculated Nernst potentials, implying that the cells were sealed well. Increasing the applied electrolysis current density leads to an increase in the voltage. At 800 and 750 °C, the nonlinear increase in the voltage at high current densities indicates potential steam starvation.³⁴ At a cell voltage of 1.3 V, the current densities of Cell A are 1.37, 1.21, and 0.88 A cm⁻² at 800, 750, and 700 °C, respectively. At 750 °C, the observed current density at 1.3 V on Cell B is almost identical to that of Cell A.

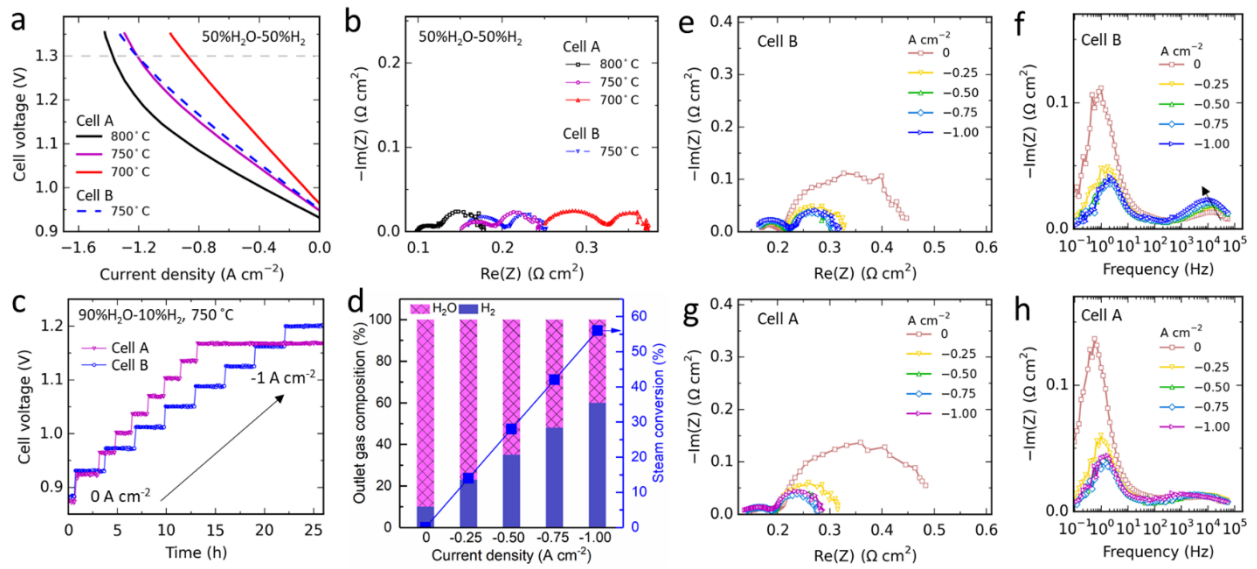


Figure 3. Performance of Cell A and Cell B for steam electrolysis. (a) *I-V* curves and (b) Nyquist plots of EIS data of the electrolysis cells measured at 800–700 °C with 50% H₂O-50% H₂ fed to the H₂-electrode and dry air to the O₂-electrode. (c) Dependence of cell voltage on applied current density for cells at 750 °C with 90% H₂O-10% H₂ fed to the H₂-electrode and pure O₂ to the O₂-electrode. (d) Corresponding gas composition at the outlet and overall steam conversion under the applied current densities. (e, g) Nyquist plots and (f, h) Bode plots of cells recorded at different current densities with 90% H₂O-10% H₂ fed to the H₂-electrode and pure O₂ to the O₂-electrode.

Figure 3b shows the Nyquist plots of the Electrochemical Impedance Spectroscopy (EIS) data recorded at open circuit condition. The total electrode polarization resistances (R_p), taken as the overall width of the depressed arcs, are determined to be 0.078, 0.089, and 0.121 $\Omega \text{ cm}^2$ for Cell A at 800, 750, and 700 $^\circ\text{C}$, respectively, and 0.092 $\Omega \text{ cm}^2$ for Cell B at 750 $^\circ\text{C}$. These R_p values are lower than those reported for most cells with Ni/YSZ H_2 -electrodes and using different O_2 -electrodes (Table S1), including the commonly used LSCF/CGO composite electrodes,³⁵⁻³⁷ as well as the infiltrated electrodes such as LSCF-YSZ,⁵ $\text{Sm}_{0.5}\text{Sr}_{0.5}\text{CoO}_{3-\delta}$ (SSC)-YSZ,³⁸ $\text{Nd}_2\text{NiO}_{4+\delta}$ - $\text{Zr}_{0.88}\text{Sc}_{0.22}\text{Ce}_{0.01}\text{O}_{2.11}$ (NNO-SSZ),⁴ $\text{La}_{0.8}\text{Sr}_{0.2}\text{Co}_{0.8}\text{Ni}_{0.2}\text{O}_{3-\delta}$ -CGO (LSCN-CGO).³⁹

The performance of the cells was further investigated by galvanostatic tests at 750 $^\circ\text{C}$ with 90% H_2O -10% H_2 fed to the H_2 -electrode and pure O_2 to the O_2 -electrode. In Figure 3c, the evolution of the cell voltage when stepping up the current density from 0 up to 1.00 A cm^{-2} is shown. Note that the production rate of H_2 is proportional to the applied current density assuming a Faraday efficiency of 100%. At 1.00 A cm^{-2} , the H_2 production rate reaches 0.448 mol cm^{-2} per day, corresponding to a steam-to-hydrogen conversion of $\sim 56\%$ and a hydrogen content of $\sim 60\%$ in the outlet gas (Figure 3d). The superiority of Cell A (with CGO-Ni/YSZ H_2 -electrode) becomes more evident with increasing current density.

Figures 3e-h compare Nyquist and Bode plots of EIS data obtained for Cell A and Cell B recorded at different current densities. The EIS response below $\sim 10^2$ Hz corresponds to the chemical processes including gas diffusion and conversion, and the EIS response in the frequency range ($\sim 10^2$ – 10^5 Hz) relates to the electrochemical processes in electrodes,⁴⁰⁻⁴¹ supported by detailed EIS analysis in Figure S3. For Cell B, increasing the current density resulted in a considerably increase of the imaginary part in the frequency range $\sim 10^2$ – 10^5 Hz and the peak

frequency shifted from $\sim 2 \times 10^4$ Hz to $\sim 9 \times 10^3$ Hz. Cell A was in the corresponding frequency range $\sim 10^2$ – 10^5 Hz much less sensitive to the increased current density. As these two cells differ only in the H₂-electrode intentionally, different behavior with respect to current dependence can be ascribed to the effect of infiltrating nanostructured CGO into the Ni/YSZ electrode. Cell A and Cell B showed a similar behavior below $\sim 10^2$ Hz with increasing current density. The changes in this frequency range can be ascribed to changes of H₂O:H₂ ratio in the H₂-electrode that affects both conversion and diffusion resistances.⁴²

Durability assessment. Durability tests were performed at 750 °C with a constant current density of 1.00 A cm⁻², and 90% H₂O-10% H₂ fed to the H₂-electrode and pure O₂ to the O₂-electrode. Figure 4a compares the evolution of cell voltage with time for the two cells. The voltage of Cell B increased from 1.200 V to 1.445 V during 537 h testing, corresponding to a degradation rate of 0.565 V kh⁻¹ (Note that the period from 194 h - 297 h where the cell was at open circuit condition has been excluded in the calculation of degradation rate). For Cell A, the cell voltage increased from 1.167 V to 1.189 V over 900 h, corresponding to a degradation rate of 0.024 V kh⁻¹, more than 20 times lower than that for Cell B.

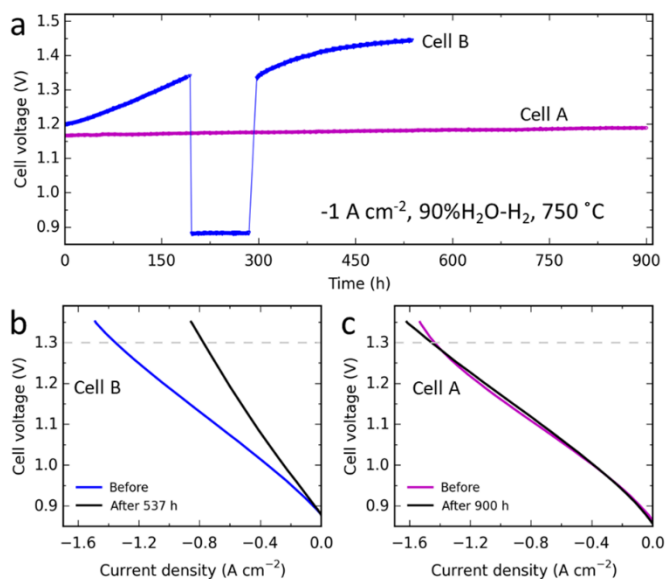


Figure 4. Comparison of the cell durability during steam electrolysis. (a) Evolution of cell voltage during long-term test under a constant current density of 1.00 A cm^{-2} at 750°C . (b, c) I - V curves collected before and after the durability tests. A $90\% \text{ H}_2\text{O}-10\% \text{ H}_2$ gas mixture was fed to the H_2 -electrode and pure O_2 was supplied to the O_2 -electrode.

The durability of Cell A is actually superior to most previously studied SOECs despite being tested at harsher conditions. As mentioned in the introduction, a degradation rate of 0.952 V kh^{-1} was reported on a conventional SOEC (Ni/YSZ support | Ni/YSZ H_2 -electrode | YSZ electrolyte | LSM/YSZ O_2 -electrode) under identical current but 50°C higher testing temperature (800°C).⁶ Besides, a degradation rate of 0.125 V kh^{-1} (i.e., 5 times that of Cell A) was reported for a Ni/YSZ H_2 -electrode supported SOEC with a thin YSZ electrolyte, and a $\text{LaNi}_{0.5}\text{Co}_{0.5}\text{O}_{3-\delta}$ infiltrated YSZ O_2 -electrode under the same high current density of 1.00 A cm^{-2} and steam conversion of 56% but at slightly higher temperature, $\sim 800^\circ \text{C}$.⁴³ A degradation rate of 0.040 V kh^{-1} (~ 2 times that of Cell A) was reported under 1.00 A cm^{-2} and a lower steam conversion of 36% and at higher temperature of $\sim 775^\circ \text{C}$ on a Ni/YSZ H_2 -electrode supported SOEC with a thin YSZ electrolyte,

a CGO barrier and a screen printed $\text{La}_{0.58}\text{Sr}_{0.4}\text{Co}_{0.2}\text{Fe}_{0.8}\text{O}_3$ O_2 -electrode.²⁴ Note that the steam conversion has significant effect on cell durability, e.g. lowering the steam conversion from 70% to 42% resulted in a decrease of degradation rate from 0.114 V kh^{-1} to 0.064 V kh^{-1} as reported in a previous work.²⁹ There is one exception; Wood's et al. reported a cell named “HiPoD” achieving a low degradation rate of 0.027 V kh^{-1} at extremely high current density of 3 A cm^{-2} at 750°C .⁴⁴ Unfortunately, only little detail on cell structure has been provided in ref⁴⁴. The I - V curves collected before and after the durability tests are shown in Figures 4b,c. The change in current density at 1.3 V also verifies the good durability of Cell A. Cell A even showed a slight increase of current density after 900 h operation. By contrast, the current density in the I - V test degraded more than 40% after 537 h for Cell B.

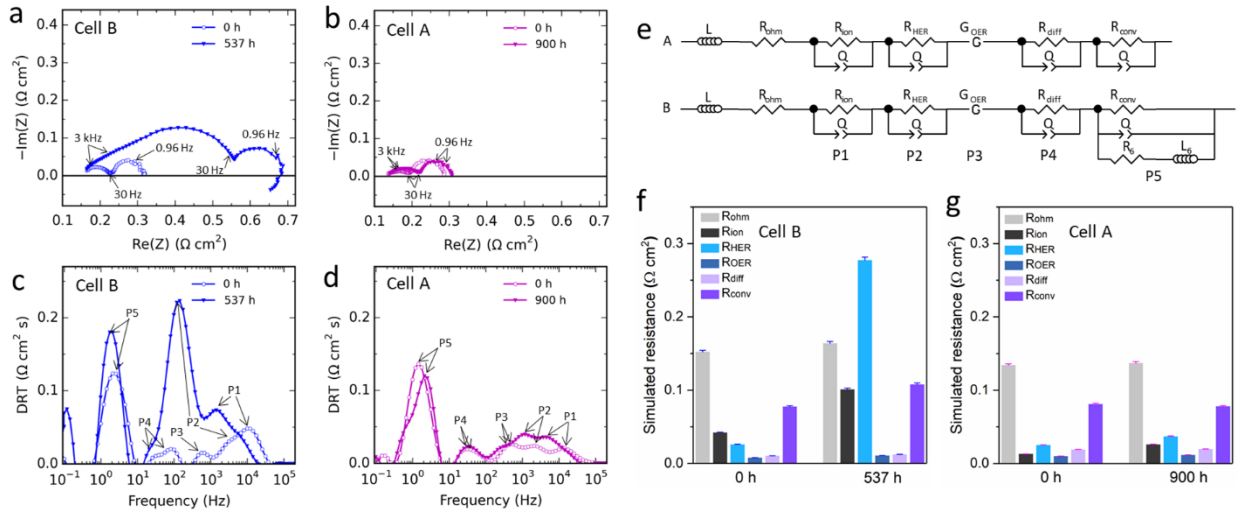


Figure 5. (a, b) Nyquist plots recorded at start and end of the durability test period. (c, d) Distribution of relaxation time for the impedance data shown in (a) and (b). (e) Electrical equivalent circuits used in the fitting. (f, g) Results from equivalent circuit best fit modeling of the impedance spectra.

Figures 5a,b show the Nyquist plots of the EIS data obtained at the start and end of the durability test period. An increase in the R_P of $\sim 0.779 \Omega \text{ cm}^2 \text{ kh}^{-1}$ is observed for Cell B, indicating significant degradation, whereas the R_P of Cell A only had a slight increase of $\sim 0.020 \Omega \text{ cm}^2 \text{ kh}^{-1}$. These results correspond well with the voltage evolution results plotted in Figure 4a.

In order to further clarify the type of contributions to R_P and their evolution over time, the distribution of relaxation time (DRT) has been calculated for the EIS data.⁴⁵ The results are shown in Figures 5c,d. For both cells, five peaks (P1, P2, P3, P4 and P5) in the frequency range from 0.3–96850 Hz were identified on the initial spectra. Each peak represents an electrochemical or chemical process in the H_2 - or O_2 -electrode, whereas the area under each peak corresponds to the magnitude of resistance for that electrode process.⁴⁶ On the basis of previously reported analyses:^{23,25,42} P1 is tentatively ascribed to the transport of oxygen anions across electrolyte-electrode interfaces and through the ionic conducting network in the electrodes. Since the applied cells have a highly ionic conducting CGO scaffold based O_2 -electrode, the major contribution of P1 could well originate from the H_2 -electrode that has a YSZ network; P2 is associated with the HER process at the triple phase boundaries (TPBs) of the H_2 -electrode; P3 is likely associated with the OER, while P4 represents the gas diffusion and P5 the gas conversion in the H_2 -electrode. For Cell B, among the five peaks, P1 and P2 increased markedly and shifted to lower frequency, indicating that the major degradation is from the Ni/YSZ H_2 -electrode. Whereas, for Cell A the P1 and P2 only revealed a slight increase; well in line with the fact that the only intended difference between the cells is on the H_2 -electrode.

To enable a quantitative analysis of the various contributions to cell degradation, these spectra were further fitted with equivalent circuit models by the complex-non-linear-least-squares (CNLS)

method.^{23,25,47} The spectrum of Cell B at 0 h and spectra of Cell A were fitted with the circuit A, while the spectrum of Cell B at 537 h was fitted with the circuit B (Figure 5e). In circuit B the R_6L_6 was added to describe the inductance loop at low frequency. This process has been shown to originate from reduction of YSZ in Ni/YSZ electrode.⁴⁷ The detailed fitting results are shown in Figures S4, S5 and Table S3. Figures 5f,g summarize the simulated values of R_{ohm} and resistances associated with each of the electrode processes. In contrast to many studies on SOECs with Ni/YSZ H₂-electrodes, in which R_{ohm} is observed to increase considerably during continuous operation at high current densities,^{14,26,48} we observed that the increase of R_{ohm} on Cell B was only 0.012 $\Omega\text{ cm}^2$ after 537 h. This is ascribed to the optimized Ni/YSZ H₂-electrode as previously discussed.²³ By introducing the nanostructured CGO coating into the Ni/YSZ H₂-electrode, the increase of R_{ohm} on Cell A was further reduced to 0.003 $\Omega\text{ cm}^2$ in 900 h. The increase of resistance for transport of oxygen anions (R_{ion} , corresponding to P1) and the resistance for the HER at the TPBs in Ni/YSZ H₂-electrode (R_{HER} , corresponding to process P2) on Cell B were 0.059 $\Omega\text{ cm}^2$ and 0.251 $\Omega\text{ cm}^2$, respectively, and contributed to ~90% of the total increase of R_P , showing that the Ni/YSZ H₂-electrode dominates the cell degradation. Cell A with the CGO-Ni/YSZ H₂-electrode had initially a lower initial R_{ion} of 0.013 $\Omega\text{ cm}^2$, less than 31% of the one found for Cell B (0.042 $\Omega\text{ cm}^2$). More importantly, the increase of R_{ion} and R_{HER} on Cell A were much less; only 0.013 $\Omega\text{ cm}^2$ and 0.012 $\Omega\text{ cm}^2$ in 900 h, respectively. These results further demonstrate that the nano-CGO coating improves significantly the electrode durability at 1 A cm⁻², as also argued from the fact that this electrode is the one that differs between the two cells. Note that the resistances for gas diffusion (R_{DIFF} , corresponding to P4) on Cell A were slightly higher than those on Cell B, which is attributed to the reduced porosity in the Ni/YSZ electrode after coating with CGO, also explaining

the stronger tendency of steam starvation (the observed nonlinearity at high current density) in the *I*-*V* measurement of Cell A (Figure 3a).

As can also be seen in Figures 5f,g, the resistances for the OER at the LSC-CGPO-CGO O₂-electrode (R_{OER} , corresponding to P3) were around 0.010 $\Omega \text{ cm}^2$ for both cells initially (0 h). These values are lower than those reported for a screen-printed LSC/CGO composite electrode tested under identical gas and current conditions but at 50 °C higher testing temperature (800 °C).²³ Furthermore, the increase of R_{OER} were as low as 0.003 $\Omega \text{ cm}^2$ on Cell B, and 0.002 $\Omega \text{ cm}^2$ on Cell A. These fitting results further confirm the good activity and stability of the LSC-CGPO-CGO O₂-electrode for the OER in SOECs operated at 1 A cm⁻². The improved electrode stability was also supported by SEM images as shown in Figure S6, where no obvious change in the microstructure of the LSC-CGPO-CGO electrodes was observed after the durability tests.

Microstructural evolution and discussion of degradation mechanisms. Figure 6 shows SEM images of the Ni/YSZ electrode in Cell B and the CGO-Ni/YSZ electrode in Cell A after the durability test. In the SEM images obtained by the low-voltage contrast technique,⁴⁹ a slight loss of Ni percolation is observed in Cell B after the durability test, particularly close to the electrode/electrolyte interface (Figure 6a), as compared with the initially pre-reduced electrode (Figure S7). In contrast, the Ni percolation in Cell A in the CGO modified electrode is practically intact. Furthermore, after the durability test, we observe clear disconnections (or gaps, or detachment) between Ni and YSZ in Cell B (Figure 6c) but none for the CGO modified electrode in Cell A (Figure 6d). High magnification images of the electrode combined with EDX characterization reveals the formation of ZrO₂ nanoparticles on the Ni grains at disconnected interfaces (Figure 6e, and Figure S8). No evidence of formation of ZrO₂ nanoparticles in the CGO

modified electrode is observed. The nano-CGO particles have clearly coarsened after the durability test, but they are still in the nanoscale with a size around 60 nm. They seem partly connected forming a surface network (Figure 6f). Based on the microstructural observations, we suggest that: the degradation mechanism on Cell B leading to the fast increase of R_{ion} and R_{HER} is the disconnection between Ni and YSZ at the TPBs, which is caused by a combined effect of Ni migration, and YSZ reduction and formation of ZrO_2 nanoparticles on the Ni surface under the high cathodic overpotential estimated to be varying from 0.066 V to 0.378 V during the durability test (see Figure 7a,b).^{19-20,47} This “disconnection” is effectively suppressed by modifying the Ni/YSZ with the nano-CGO coating. The slight increase in R_{ion} and R_{HER} of Cell A is likely due to the coarsening of the nano-CGO. The above results further confirm that the present nano-CGO-Ni/YSZ architecture is highly active for the HER and demonstrates great promise as an efficient and robust H_2 -electrode for steam electrolysis in SOECs.

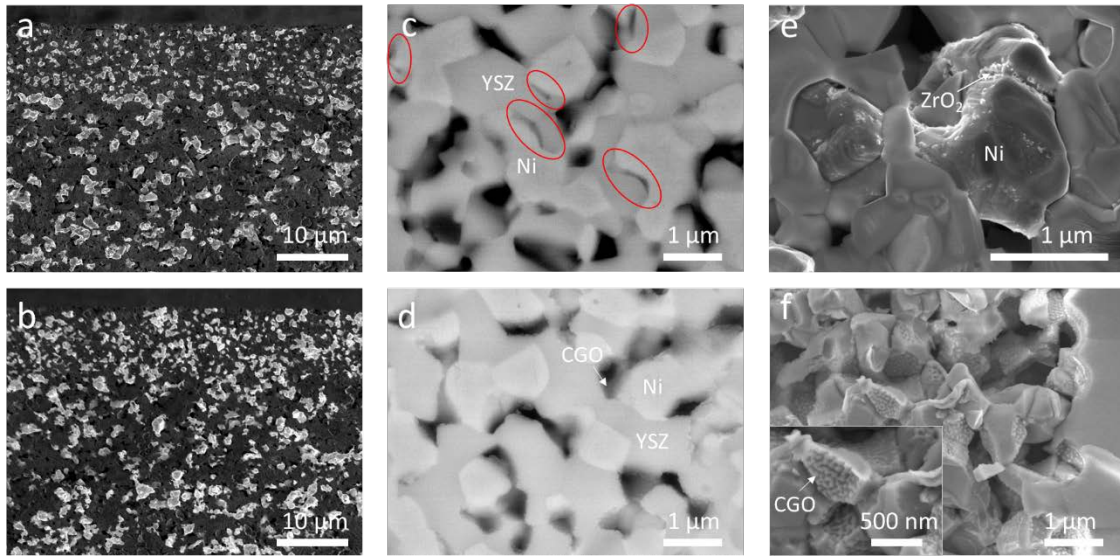


Figure 6. SEM characterization of the H_2 -electrode in Cell B and Cell A after the durability test. SEM images showing Ni percolation in (a) the Ni/YSZ H_2 -electrode and (b) the CGO-Ni/YSZ H_2 -

electrode. SEM images of polished cross-sections showing the Ni-YSZ interface in (c) the Ni/YSZ H₂-electrode and (d) the CGO modified electrode. SEM images showing fracture surface of (e) the Ni/YSZ H₂-electrode and (f) the CGO modified one. The inset is an image with high resolution.

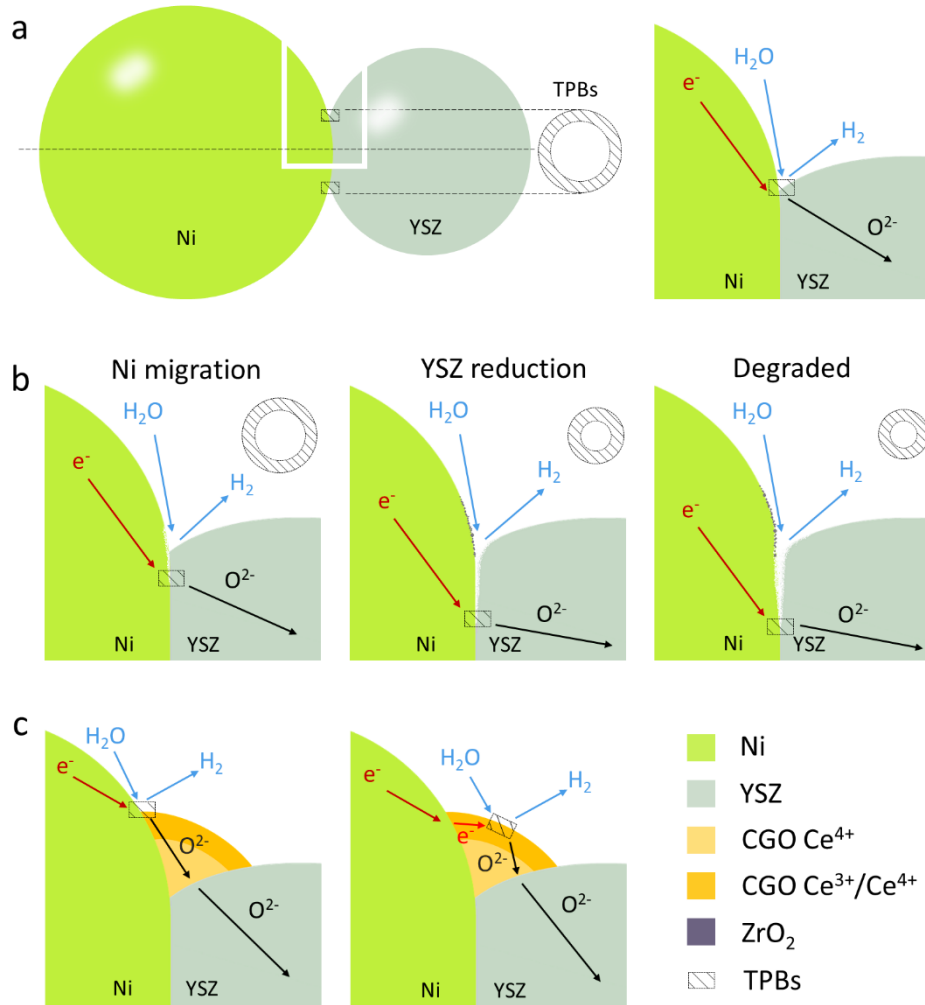
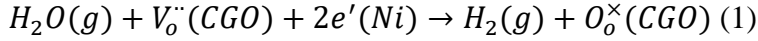


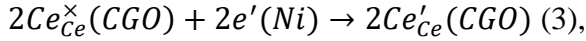
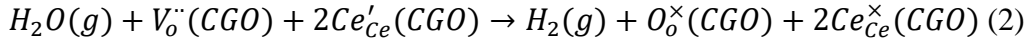
Figure 7. (a) Schematic illustration of the HER reaction at the three-phase boundary (TPB) in the Ni/YSZ electrode and (b) the suggested mechanism of microstructural deterioration of the electrode during high-current-density electrolysis operation. (c) Mitigation of the discussed mechanism by CGO modification.

It has been demonstrated that the CGO can act as catalyst for dissociation of H₂O.⁵⁰⁻⁵¹ Furthermore, the CGO will under the applied electrolysis conditions show mixed electronic and oxygen ion conductivity.⁵² Therefore, introducing such a CGO coating into the Ni/YSZ electrode presumably provides additional active sites for the HER (Figure 7c),⁵³ e.g., TPBs at the nano-CGO, Ni and gas interface (Ni-CGO-gas); and at the two-phase boundary (2PB) at the surface of the CGO located on Ni grains (CGO-gas), thereby enhancing activity and structural stability. The reaction at these sites with nano-CGO may proceed in multiple consecutive or parallel steps as follows:

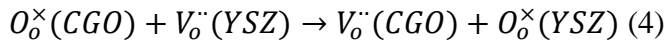
Dissociation of H₂O molecules at Ni-CGO-gas interface



or at the CGO-gas interface



and finally transport of oxygen vacancies within CGO coatings and transfer to YSZ



Where $V_o^{\bullet\bullet}(YSZ \text{ or } CGO)$ and $O_o^{\times}(YSZ \text{ or } CGO)$ represent oxygen ions and oxygen vacancies in the YSZ or CGO lattice, respectively. Compared to the YSZ in Ni/YSZ that has been sintered at 1315 °C, the more active surface oxygen exchange kinetics and excellent surface oxygen redox capacity of the nano-CGO is likely to facilitate the dissociation of H₂O molecules and the charge

transfer process, thus significantly enhancing the durability of the Ni/YSZ H₂-electrode under high current loading. Future work on electrocatalytic activity of steam splitting on CGO using density-functional theory (DFT) calculation may help to prove this.

Conclusion

In summary, we demonstrated that planar SOECs incorporating two nano-engineered electrodes (a LSC-CGPO-CGO O₂-electrode and a CGO modified Ni/YSZ H₂-electrode) prepared via conventional techniques of ceramic processing and chemical infiltration, exhibit both excellent initial performance at 750 °C and decent long-term durability at high current density of 1 A cm⁻², when tested at a technologically relevant level of 4×4 cm² (active area). The low R_{OER} resistance of 0.012 Ω cm² after 900 h operation and no obvious change in the microstructure suggest that the nanostructured LSC-CGPO-CGO is highly active and durable for the OER, which demonstrates the potential of designing robust O₂-electrode via infiltration for large-scale manufacture of SOECs. The introduced CGO coating effectively mitigates the microstructural deterioration (typically disconnection between Ni and YSZ at the TPBs) seen on non-modified Ni/YSZ electrodes under these conditions, thus significantly enhancing cell durability. These findings represent an important advance towards development of long-term stable SOECs, and improve the commercial feasibility of integrating SOEC technology into sustainable energy future.

Experimental Methods

Preparation of the LSC-CGPO-CGO O₂-electrode. The inner surface of the porous CGO scaffold was first infiltrated with 0.7 M Gd,Pr co-doped CeO₂ (CGPO) nitrate solution containing stoichiometric amounts of Ce(NO₃)₃, Gd(NO₃)₃, and Pr(NO₃)₃ (16:4:5 molar ratio to metal ions),

followed by calcination at 350°C in air for 15 min. The Triton X-100 surfactant (0.7 wt. %) was added into the CGPO solution to improve wetting/penetration of the structure. The infiltration was performed by dripping the CGPO solution onto the surface of the CGO scaffold. The solution will cover and wet all the surface due to the capillary force, and then the solution will be sucked into the scaffold. After 30 seconds, the residual solution was wiped off from the surface. The loading of CGPO was ~ 111 mg per 1 cm^3 CGO scaffold. Hereafter, the scaffold was further infiltrated with a 0.5 M LSC nitrate solution containing stoichiometric amounts of $\text{La}(\text{NO}_3)_3$, $\text{Sr}(\text{NO}_3)_2$, and $\text{Co}(\text{NO}_3)_3$ (3:2:5 molar ratio of $\text{La}^{3+}:\text{Sr}^{2+}:\text{Co}^{3+}$), followed by calcination. The Pluronic P-123 surfactant (1.7 wt. %) was added into the LSC solution.⁵⁴ The infiltration of LSC and the following calcination processes were repeated 9 times to get a loading of ~ 1185 mg per 1 cm^3 CGO scaffold. Finally, a LSC current-collector layer was applied on the top of the O_2 -electrode by screen-printing.

Preparation of the CGO-Ni/YSZ H_2 -electrode. The NiO/YSZ electrode was reduced by a “one sided” reduction in a specific in-house rig at 850 °C, with 24 l/h $\text{H}_2\text{O}/\text{H}_2$ (4/96) fed to the Ni/YSZ H_2 -electrode and 50 l/h dry air to the O_2 -electrode. Afterwards, the pre-reduced Ni/YSZ was infiltrated with a 0.3 M CGO nitrate solution containing stoichiometric amounts of $\text{Ce}(\text{NO}_3)_3$ and $\text{Gd}(\text{NO}_3)_3$ (4:2 molar ratio to metal ions), followed by calcination at 300°C in air for 15 min. The PE-L62 surfactant (1.4 wt. %) was added into the CGO solution.²⁹ The infiltration processes were repeated 7 times to get a loading of 120 mg CGO per 1 cm^3 Ni/YSZ structure (Ni/YSZ H_2 -electrode + Ni/YSZ support).

Electrochemical performance and durability testing of the cells. The electrochemical performance and durability of the cells were tested via in-house testing rigs, as described in previous work.^{42,55} For all the tests, the cells were mounted and sealed to an alumina housing.

Corrugated nickel mesh and nickel plate were used as the contact components on the H₂-electrode side. Corrugated gold mesh and gold plate were used on the O₂-electrode side. A gold frame was used for sealing on H₂-electrode side. To ensure a good seal and a good electrical contact, four kilograms of weight was applied on top of the cell house during start up. The cells were heated (1 °C min⁻¹) to 800 °C for sealing with 9 % H₂ in Ar to H₂-electrodes and air to O₂-electrodes for 2 h, followed by another 2 h with humidified H₂ (4 % H₂O) to H₂-electrodes. Meanwhile, this reduction process will enable the infiltrated materials to form desired crystalline phases. The electrochemical performance of the cells was characterized at 800–700 °C. A Solartron 1255 frequency response analyzer in combination with a measurement resistor was used for recording EIS, at frequencies from 96850 to 0.0968 Hz with an amplitude of 3.75 mA cm⁻². The galvanostatic durability tests were conducted at 750 °C, with 50 l/h pure oxygen supplied to the O₂-electrode and 13.4 l/h 90% H₂O-10% H₂ to the H₂-electrode under a constant current density of 1 A cm⁻². The EIS spectra were also measured during the durability testing period. The in-house developed Python-based software Ravdav was used for plotting and analysis of the EIS data.⁵⁶

Microstructure characterization. The cross-section of cells were examined using a Zeiss Merlin scanning electron microscope (SEM). For the fractured samples an accelerating voltage of 5 kV was used. To examine the percolation of Ni in Ni/YSZ electrodes, a low-voltage of 1 kV and an Inlens secondary electron detector in the SEM were used.⁴⁹ For the polished samples, they were first coated with carbon, and analyzed at an accelerating voltage of 15 kV. For energy-dispersive X-ray spectroscopy (EDX) analysis, an accelerating voltage of 10 kV was used in Figure S1 and a voltage of 5 kV was used in Figure S8.

ASSOCIATED CONTENT

Supporting Information.

The Supporting Information is available free of charge on the ACS Publications website at DOI:.

- Tables summarizing the performance of the solid oxide electrolysis cells from literature and from the current work, photo of the as-prepared Cell A, SEM, EDX elemental mappings, EIS spectra, CNLS fits of spectra, Table summarizing the fitting results

AUTHOR INFORMATION

Corresponding Author

*E-mail: minc@dtu.dk

ORCID

Xiaofeng Tong: 0000-0003-2227-7441

Simona Ovtar: 0000-0003-4588-2679

Peter Vang Hendriksen: 0000-0002-4748-532X

Ming Chen: 0000-0001-6387-3739

Notes

The authors declare no competing financial interest.

ACKNOWLEDGMENT

The authors gratefully acknowledge funding from Danish TSO – Energinet.dk through the project “Towards Solid Oxide Electrolysis Plants in 2020” (ForskEL 2015-1-12276) and from EUDP through the project “Efficient Power2Gas Combining SOEC and Biomass Gasification” (EUDP no. 64017-0011). X. F. Tong acknowledges financial support from the China Scholarship Council (201604910912). The authors are also grateful towards H. Henriksen and M. Davodi for help with experimental work on the cell testing, A. Hauch for help with impedance analysis, and E. Abdellahi for help with SEM sample preparation.

REFERENCES

- (1) Glenk, G.; Reichelstein, S. Economics of Converting Renewable Power to Hydrogen. *Nat. Energy* **2019**, *4* (3), 216-222.
- (2) Zhang, S.-L.; Wang, H.; Lu, M. Y.; Zhang, A.-P.; Mogni, L. V.; Liu, Q.; Li, C.-X.; Li, C.-J.; Barnett, S. A. Cobalt-Substituted $\text{SrTi}_{0.3}\text{Fe}_{0.7}\text{O}_{3-\delta}$: A Stable High-Performance Oxygen Electrode Material for Intermediate-Temperature Solid Oxide Electrochemical Cells. *Energy Environ. Sci.* **2018**, *11* (7), 1870-1879.
- (3) Laguna-Bercero, M. A. Recent Advances in High Temperature Electrolysis Using Solid Oxide Fuel Cells: A Review. *J Power Sources* **2012**, *203*, 4-16.
- (4) Chen, T.; Liu, M.; Yuan, C.; Zhou, Y.; Ye, X.; Zhan, Z.; Xia, C.; Wang, S. High Performance of Intermediate Temperature Solid Oxide Electrolysis Cells Using $\text{Nd}_2\text{NiO}_{4+\delta}$ Impregnated Scandia Stabilized Zirconia Oxygen Electrode. *J Power Sources* **2015**, *276*, 1-6.
- (5) Fan, H.; Keane, M.; Li, N.; Tang, D.; Singh, P.; Han, M. Electrochemical Stability of $\text{La}_{0.6}\text{Sr}_{0.4}\text{Co}_{0.2}\text{Fe}_{0.8}\text{O}_{3-\delta}$ -Infiltrated YSZ Oxygen Electrode for Reversible Solid Oxide Fuel Cells. *Int. J. Hydrogen Energy* **2014**, *39* (26), 14071-14078.
- (6) Graves, C.; Ebbesen, S. D.; Jensen, S. H.; Simonsen, S. B.; Mogensen, M. B. Eliminating Degradation in Solid Oxide Electrochemical Cells by Reversible Operation. *Nat. Mater.* **2015**, *14* (2), 239-244.
- (7) Hartvigsen, J.; Elangovan, S.; O'Brien, J.; Stoots, C.; Herring, J. S.; Lessing, P. Operation and Analysis of Sofcs in Steam Electrolysis Mode, *6th European Solid Oxide Fuel Cell Forum*, Lucerne, Switzerland, 2004; pp 378-387.
- (8) Chen, K. F.; Ai, N.; Jiang, S. P. Performance and Stability of $(\text{La,Sr})\text{MnO}_3\text{-Y}_2\text{O}_3\text{-ZrO}_2$ Composite Oxygen Electrodes under Solid Oxide Electrolysis Cell Operation Conditions. *Int. J. Hydrogen Energy* **2012**, *37* (14), 10517-10525.
- (9) Tao, Y. K.; Ebbesen, S. D.; Mogensen, M. B. Degradation of Solid Oxide Cells During Co-Electrolysis of Steam and Carbon Dioxide at High Current Densities. *J Power Sources* **2016**, *328*, 452-462.
- (10) Laguna-Bercero, M. A.; Kilner, J. A.; Skinner, S. J. Performance and Characterization of $(\text{La,Sr})\text{MnO}_3/\text{YSZ}$ and $\text{La}_{0.6}\text{Sr}_{0.4}\text{Co}_{0.2}\text{Fe}_{0.8}\text{O}_3$ Electrodes for Solid Oxide Electrolysis Cells. *Chem. Mater.* **2010**, *22* (3), 1134-1141.
- (11) Kim, J.; Ji, H. I.; Dasari, H. P.; Shin, D.; Song, H.; Lee, J. H.; Kim, B. K.; Je, H. J.; Lee, H. W.; Yoon, K. J. Degradation Mechanism of Electrolyte and Air Electrode in Solid Oxide Electrolysis Cells Operating at High Polarization. *Int. J. Hydrogen Energy* **2013**, *38* (3), 1225-1235.
- (12) Hughes, G. A.; Railsback, J. G.; Yakal-Kremski, K. J.; Butts, D. M.; Barnett, S. A. Degradation of $(\text{La}_{0.8}\text{Sr}_{0.2})_{0.98}\text{MnO}_{3-\delta}\text{-Zr}_{0.84}\text{Y}_{0.16}\text{O}_{2-\gamma}$ Composite Electrodes During Reversing Current Operation. *Faraday Discuss.* **2015**, *182*, 365-377.
- (13) Hughes, G. A.; Yakal-Kremski, K.; Barnett, S. A. Life Testing of LSM-YSZ Composite Electrodes under Reversing-Current Operation. *Phys Chem Chem Phys* **2013**, *15* (40), 17257-17262.
- (14) Knibbe, R.; Traulsen, M. L.; Hauch, A.; Ebbesen, S. D.; Mogensen, M. Solid Oxide Electrolysis Cells: Degradation at High Current Densities. *J. Electrochem. Soc.* **2010**, *157* (8), B1209-B1217.

- (15) Keane, M.; Mahapatra, M. K.; Verma, A.; Singh, P. LSM-YSZ Interactions and Anode Delamination in Solid Oxide Electrolysis Cells. *Int. J. Hydrogen Energy* **2012**, *37* (22), 16776-16785.
- (16) Ding, D.; Li, X. X.; Lai, S. Y.; Gerdes, K.; Liu, M. L. Enhancing SOFC Cathode Performance by Surface Modification through Infiltration. *Energy Environ. Sci.* **2014**, *7* (2), 552-575.
- (17) Vohs, J. M.; Gorte, R. J. High-Performance SOFC Cathodes Prepared by Infiltration. *Adv. Mater.* **2009**, *21* (9), 943-956.
- (18) Connor, P. A.; Yue, X. L.; Savaniu, C. D.; Price, R.; Triantafyllou, G.; Cassidy, M.; Kerherve, G.; Payne, D. J.; Maher, R. C.; Cohen, L. F.; Tomov, R. I.; Glowacki, B. A.; Kumar, R. V.; Irvine, J. T. S. Tailoring Sofc Electrode Microstructures for Improved Performance. *Adv. Energy Mater.* **2018**, *8* (23), 1800120.
- (19) Irvine, J. T. S.; Neagu, D.; Verbraeken, M. C.; Chatzichristodoulou, C.; Graves, C.; Mogensen, M. B. Evolution of the Electrochemical Interface in High-Temperature Fuel Cells and Electrolysers. *Nat. Energy* **2016**, *1*, 15014.
- (20) Chen, M.; Liu, Y. L.; Bentzen, J. J.; Zhang, W.; Sun, X.; Hauch, A.; Tao, Y.; Bowen, J. R.; Hendriksen, P. V. Microstructural Degradation of Ni/YSZ Electrodes in Solid Oxide Electrolysis Cells under High Current. *J. Electrochem. Soc.* **2013**, *160* (8), F883-F891.
- (21) Chen, M.; Sun, X.; Chatzichristodoulou, C.; Koch, S.; Hendriksen, P. V.; Mogensen, M. B. Thermoneutral Operation of Solid Oxide Electrolysis Cells in Potentiostatic Mode. *ECS Trans.* **2017**, *78* (1), 3077-3088.
- (22) Ebbesen, S. D.; Sun, X.; Mogensen, M. B. Understanding the Processes Governing Performance and Durability of Solid Oxide Electrolysis Cells. *Faraday Discuss.* **2015**, *182*, 393-422.
- (23) Hauch, A.; Brodersen, K.; Chen, M.; Mogensen, M. B. Ni/YSZ Electrodes Structures Optimized for Increased Electrolysis Performance and Durability. *Solid State Ionics* **2016**, *293*, 27-36.
- (24) The, D.; Grieshammer, S.; Schroeder, M.; Martin, M.; Al Daroukh, M.; Tietz, F.; Schefold, J.; Brisse, A. Microstructural Comparison of Solid Oxide Electrolyser Cells Operated for 6100 h and 9000 h. *J Power Sources* **2015**, *275*, 901-911.
- (25) Hauch, A.; Marchese, M.; Lanzini, A.; Graves, C. Re-Activation of Degraded Nickel Cermet Anodes - Nano-Particle Formation Via Reverse Current Pulses. *J Power Sources* **2018**, *377*, 110-120.
- (26) Hjalmarsson, P.; Sun, X.; Liu, Y.-L.; Chen, M. Durability of High Performance Ni-Yttria Stabilized Zirconia Supported Solid Oxide Electrolysis Cells at High Current Density. *J Power Sources* **2014**, *262*, 316-322.
- (27) Nechache, A.; Boukamp, B. A.; Cassir, M.; Ringuedé, A. Premature Degradation Study of a Cathode-Supported Solid Oxide Electrolysis Cell. *J Solid State Electr* **2018**, *23* (1), 109-123.
- (28) Tietz, F.; Sebold, D.; Brisse, A.; Schefold, J. Degradation Phenomena in a Solid Oxide Electrolysis Cell after 9000 h of Operation. *J Power Sources* **2013**, *223*, 129-135.
- (29) Ovtar, S.; Tong, X.; Bentzen, J. J.; Thyden, K. T. S.; Simonsen, S. B.; Chen, M. Boosting the Performance and Durability of Ni/YSZ Cathode for Hydrogen Production at High Current Densities via Decoration with Nano-Sized Electrocatalysts. *Nanoscale* **2019**, *11* (10), 4394-4406.
- (30) Samson, A. J.; Sogaard, M.; Bonanos, N. Electrodes for Solid Oxide Fuel Cells Based on Infiltration of Co-Based Materials. *Electrochem Solid St* **2012**, *15* (4), B54-B56.
- (31) Paier, J.; Penschke, C.; Sauer, J. Oxygen Defects and Surface Chemistry of Ceria: Quantum Chemical Studies Compared to Experiment. *Chem. Rev.* **2013**, *113* (6), 3949-3985.

- (32) Gopal, C. B.; El Gabaly, F.; McDaniel, A. H.; Chueh, W. C. Origin and Tunability of Unusually Large Surface Capacitance in Doped Cerium Oxide Studied by Ambient-Pressure X-Ray Photoelectron Spectroscopy. *Adv. Mater.* **2016**, 28 (23), 4692-4697.
- (33) Sun, C. W.; Li, H.; Chen, L. Q. Nanostructured Ceria-Based Materials: Synthesis, Properties, and Applications. *Energy Environ. Sci.* **2012**, 5 (9), 8475-8505.
- (34) Yang, C.; Yang, Z.; Jin, C.; Liu, M.; Chen, F. High Performance Solid Oxide Electrolysis Cells Using $\text{Pr}_{0.8}\text{Sr}_{1.2}(\text{Co},\text{Fe})_{0.8}\text{Nb}_{0.2}\text{O}_{4+\delta}$ -Co-Fe Alloy Hydrogen Electrodes. *Int. J. Hydrogen Energy* **2013**, 38 (26), 11202-11208.
- (35) Zhan, Z.; Kobsiriphat, W.; Wilson, J. R.; Pillai, M.; Kim, I.; Barnett, S. A. Syngas Production by Coelectrolysis of $\text{CO}_2/\text{H}_2\text{O}$: The Basis for a Renewable Energy Cycle. *Energy Fuels* **2009**, 23 (6), 3089-3096.
- (36) Lopez-Robledo, M. J.; Laguna-Bercero, M. A.; Larrea, A.; Orera, V. M. Reversible Operation of Microtubular Solid Oxide Cells Using $\text{La}_{0.6}\text{Sr}_{0.4}\text{Co}_{0.2}\text{Fe}_{0.8}\text{O}_{3-\delta}$ - $\text{Ce}_{0.9}\text{Gd}_{0.1}\text{O}_{2-\delta}$ Oxygen Electrodes. *J Power Sources* **2018**, 378, 184-189.
- (37) Lee, S.-i.; Kim, J.; Son, J.-W.; Lee, J.-H.; Kim, B.-K.; Je, H.-J.; Lee, H.-W.; Song, H.; Yoon, K. J. High Performance Air Electrode for Solid Oxide Regenerative Fuel Cells Fabricated by Infiltration of Nano-Catalysts. *J Power Sources* **2014**, 250, 15-20.
- (38) Fan, H.; Han, M. Electrochemical Stability of $\text{Sm}_{0.5}\text{Sr}_{0.5}\text{CoO}_{3-\delta}$ -Infiltrated YSZ for Solid Oxide Fuel Cells/Electrolysis Cells. *Faraday Discuss.* **2015**, 182, 477-491.
- (39) Tan, Y.; Wang, A.; Jia, L.; Yan, D.; Chi, B.; Pu, J.; Li, J. High-Performance Oxygen Electrode for Reversible Solid Oxide Cells with Power Generation and Hydrogen Production at Intermediate Temperature. *Int. J. Hydrogen Energy* **2017**, 42 (7), 4456-4464.
- (40) Graves, C.; Ebbesen, S. D.; Mogensen, M. Co-Electrolysis of CO_2 and H_2O in Solid Oxide Cells: Performance and Durability. *Solid State Ionics* **2011**, 192 (1), 398-403.
- (41) Barfod, R.; Mogensen, M.; Klemenso, T.; Hagen, A.; Liu, Y. L.; Hendriksen, P. V. Detailed Characterization of Anode-Supported SOFCs by Impedance Spectroscopy. *J. Electrochem. Soc.* **2007**, 154 (4), B371-B378.
- (42) Jensen, S. H.; Hauch, A.; Hendriksen, P. V.; Mogensen, M. Advanced Test Method of Solid Oxide Cells in a Plug-Flow Setup. *J. Electrochem. Soc.* **2009**, 156 (6), B757-B764.
- (43) Chrzan, A.; Ovtar, S.; Jasinski, P.; Chen, M.; Hauch, A. High Performance $\text{LaNi}_{1-x}\text{Co}_x\text{O}_{3-\delta}$ ($x = 0.4$ to 0.7) Infiltrated Oxygen Electrodes for Reversible Solid Oxide Cells. *J Power Sources* **2017**, 353, 67-76.
- (44) Wood, T.; He, H.; Joia, T.; Mark, K.; Steedman, D.; Tang, E.; Brown, C.; Luc, K. Solid Oxide Electrolysis Development at Versa Power Systems, *12th European SOFC & SOE Forum*, Lucerne/Switzerland, 2016; pp 184-191.
- (45) Leonide, A.; Sonn, V.; Weber, A.; Ivers-Tiffée, E. Evaluation and Modeling of the Cell Resistance in Anode-Supported Solid Oxide Fuel Cells. *J. Electrochem. Soc.* **2008**, 155 (1), B36-B41.
- (46) Zhang, X.; Liu, L.; Zhao, Z.; Tu, B.; Ou, D.; Cui, D.; Wei, X.; Chen, X.; Cheng, M. Enhanced Oxygen Reduction Activity and Solid Oxide Fuel Cell Performance with a Nanoparticles-Loaded Cathode. *Nano Lett.* **2015**, 15 (3), 1703-1709.
- (47) Hansen, K. V.; Chen, M.; Jacobsen, T.; Thydén, K.; Simonsen, S. B.; Koch, S.; Mogensen, M. B. Effects of Strong Cathodic Polarization of the Ni-YSZ Interface. *J. Electrochem. Soc.* **2016**, 163 (10), F1217-F1227.

- (48) Ebbesen, S. D.; Jensen, S. H.; Hauch, A.; Mogensen, M. B. High Temperature Electrolysis in Alkaline Cells, Solid Proton Conducting Cells, and Solid Oxide Cells. *Chem. Rev.* **2014**, *114* (21), 10697-10734.
- (49) Thyden, K. Microstructural Characterization of SOFC Ni-YSZ Anode Composites by Low-Voltage Scanning Electron Microscopy. *Solid State Ionics* **2008**, *178* (39-40), 1984-1989.
- (50) Le Gal, A.; Abanades, S. Dopant Incorporation in Ceria for Enhanced Water-Splitting Activity During Solar Thermochemical Hydrogen Generation. *J. Phys. Chem. C* **2012**, *116* (25), 13516-13523.
- (51) Wu, T.; Deng, Q.; Hansen, H. A.; Vegge, T. Mechanism of Water Splitting on Gadolinium-Doped CeO₂(111): A DFT + U Study. *J. Phys. Chem. C* **2019**, *123* (9), 5507-5517.
- (52) Chueh, W. C.; Falter, C.; Abbott, M.; Scipio, D.; Furler, P.; Haile, S. M.; Steinfeld, A. High-Flux Solar-Driven Thermochemical Dissociation of CO₂ and H₂O Using Nonstoichiometric Ceria. *Science* **2010**, *330* (6012), 1797-1801.
- (53) Papaefthimiou, V.; Niakolas, D. K.; Paloukis, F.; Teschner, D.; Knop-Gericke, A.; Haevecker, M.; Zafeiratos, S. Operando Observation of Nickel/Ceria Electrode Surfaces During Intermediate Temperature Steam Electrolysis. *J. Catal.* **2017**, *352*, 305-313.
- (54) Ovtar, S.; Hauch, A.; Veltzé, S.; Chen, M. Comparison between La_{0.6}Sr_{0.4}CoO_{3-δ} and LaNi_{0.6}Co_{0.4}O_{3-δ} Infiltrated Oxygen Electrodes for Long-Term Durable Solid Oxide Fuel Cells. *Electrochim. Acta* **2018**, *266*, 293-304.
- (55) Ebbesen, S. D.; Graves, C.; Hauch, A.; Jensen, S. H.; Mogensen, M. Poisoning of Solid Oxide Electrolysis Cells by Impurities. *J. Electrochem. Soc.* **2010**, *157* (10), B1419-B1429.
- (56) Graves, C. *Ravdav, Data Analysis Software, Ver 0.97, 2012.*

Graphical Abstract

